Granular Friction, Coulomb Failure, and the Fluid-Solid Transition for Horizontally Shaken Granular Materials

Guy Metcalfe
CSIRO Thermal & Fluids Engineering, Melbourne, VIC 3190, Australia

S.G.K. Tennakoon
Center for Nonlinear and Complex Systems and Physics Department, Duke University, Durham NC, 27708-0305, USA

L. Kondic
Mathematics Department, New Jersey Institute of Technology, Newark NJ 07102, USA

D.G. Schaeffer
Center for Nonlinear and Complex Systems and Mathematics Department, Duke University, Durham NC 27708, USA

R. P. Behringer
Center for Nonlinear and Complex Systems and Physics Department, Duke University, Durham NC, 27708-0305, USA
(November 15, 2001)

Abstract

We present the results of an extensive series of experiments, molecular dynamics simulations, and models that address horizontal shaking of a layer of granular material. The goal of this work was to better understand the transition between the 'fluid' and 'solid' states of granular materials. In the experiments, the material—consisting of glass spheres, smooth and rough sand—was contained in a container of rectangular cross section, and subjected to horizontal shaking of the form $x = A\sin(\omega t)$. The base of the container was porous, so that it was possible to reduce the effective weight of the sample by means of a vertical gas flow. The acceleration of the shaking could be precisely controlled by means of an accelerometer mounted onboard the shaker, plus feedback control and lockin detection. The relevant control parameter for this system was the dimensionless acceleration, $\Gamma = A\omega^2/g$, where g was the acceleration of gravity.

As Γ was varied, the layer underwent a backward bifurcation between a solid-like state that was stationary in the frame of the shaker, and a fluid-like state that typically consisted of a moving/sloshing layer of maximum depth H riding on top of a solid layer. That is, with increasing Γ, the solid state made a transition to the fluid state at Γ_{cu} and once the system was in the fluid state, a decrease in Γ left the system in the fluidized state until Γ reached $\Gamma_{cd} < \Gamma_{cu}$. In the fluidized state, the flow consisted of back and forth sloshing at the shaker frequency, plus a slower convective flow along the shaking direction and additionally in the horizontal direction transverse to the shaking direction. Molecular dynamics simulations show that the last of these flows is associated with shear and dilation at the vertical sidewalls. For $\Gamma < \Gamma_{cu}$ and in the solid state, there was a 'gas' of free particles sliding on the surface of the material. These constituted much less than one layer's worth of particles in all cases. If these 'sliders' were suppressed by placing a thin strip of plastic on the surface, the hysteresis was removed, and the transition to fluidization occurred at a slightly lower value than Γ_{cd} for the free surface case. The hysteresis was also suppressed if a vertical gas flow from the base was sufficient to support roughly 40% of the weight of the sample.

Both the transition to the fluid state from the solid and the reverse transition from the fluid to the solid were characterized by similar divergent time scales. If Γ was increased above Γ_{cu} by a fractional amount $\epsilon = (\Gamma - \Gamma_{cu})/\Gamma_{cu}$, where ϵ was small, there was a characteristic time $\tau = A\epsilon^{-\beta}$, for the transition from solid to fluid to occur, where β is 1.00 ± 0.06. Similarly, if Γ was decreased below Γ_{cd} in the fluidized state by an amount $\epsilon = (\Gamma - \Gamma_{cd})/\Gamma_{cd}$, there was also a transient time $\tau = B\epsilon^{-\beta}$, where β is again indistinguishable from 1.00. In addition, the amplitudes A and B are essentially identical. By placing a small 'impurity' on top of the layer, consisting of a heavier particle, we found that the exponent β varied as the impurity mass squared and changed by a factor of 3.

A simple Coulomb friction model with friction coefficients $\mu_k < \mu_s$ for the fluid and solid states predicts a reversible rather than hysteretic transition to the fluid state, similar to what we observe with the addition of the small overload from a plastic strip. In an improved model, we provide a relaxational mechanism that allows the friction coefficient to change continuously between the low and high values. This model produces the hysteresis seen in experiments.

PACS numbers: 46.10.+z, 47.20.-k

I. INTRODUCTION

Granular materials have been the focus of considerable recent interest, as discussed in a number of reviews and collections of papers [1]. An important aspect of granular materials concerns the transition from a compact, rigid solid-like state to a fluid-like state, and the reverse transition from fluid to solid. Solid-fluid granular transitions occur broadly in natural and commercial processes. Examples in nature include avalanches, mudslides, and ice

floes. In commercial processes, this transition occurs at the outlet of hoppers, in chute flows, vibration devices, and under other conditions where flow is necessary.

These transitions are intimately connected to Coulomb friction for granular materials and with the solid-on-solid (SoS) friction of grains rubbing against each other. They are also connected to Reynolds dilatancy–i.e. the fact that a densely packed granular sample must expand if the sample is to deform. The inverse process of compaction occurs as a dilated or fluidized granular sample coalesces into a solidified state. The current understanding of the solid and fluid states comes from two rather disjoint models: continuum models [2] such as those used in soil mechanics, and kinetic theory models [3].

The standard Mohr-Coulomb failure criterion of soil mechanics predicts failure of a granular layer when the ratio of the shear stresses to the normal stresses exceeds an appropriate factor. In general, failure should occur along surfaces where this condition is met.

In a dilated, energetic state, kinetic theory models, and more sophisticated Chapman-Enskog theories describe the material as a "granular gas". The ordinary thermodynamic temperature is replaced by the granular temperature, T_g, which is proportional to the mean fluctuating part of the granular kinetic energy. The hydrodynamics of granular materials in this representation are nearly the same as those for a conventional Newtonian fluid, except for an additional term in the energy equation due to collisional energy losses. Additionally, the transport coefficients and equation of state must reflect the properties of a granular system. At present, there is no well established unifying model that describes the nonequilibrium processes involved during the phase change between solid and fluid-like behavior and vice-versa, although a step towards a unification of the two approaches has been taken by Savage [4].

The goal of the present experiments and models is to help fill the gap by characterizing in detail the transition that occurs between solid and fluid granular states when a granular material is subject to horizontal shaking. Specifically, in the experiments described here, the material rests within a rectangular container that is subject to oscillations of the form

$$x = A\sin(\omega t). \tag{1}$$

A key parameter is then the peak acceleration, $a = A\omega^2$, or in dimensionless form

$$\Gamma \equiv A\omega^2/g, \tag{2}$$

where g is the acceleration of gravity. When $\Gamma > \mu$, or when $a > \mu g$, where μ is an appropriate friction coefficient, the Mohr-Coulomb picture of failure indicates that slipping will occur. The idea behind the present experiments is to provide an environment in which slipping can be sustained and hence studied in detail. More precisely, this environment provides a method to study the transitions between the solid and fluid granular states. We also use fully three-dimensional discrete element or molecular dynamics (MD) techniques to study aspects of the flow that occur once the material has made the transition to the fluid state.

Several other groups or individuals have probed the dynamics of granular materials subject to horizontal shaking. This work includes studies by Evesque [8], Ristow et al. [11], Liffman et al. [10], Salueña et al. [7] and Medved et al. [6]. The work by Ristow et al., Liffman et al., and Salueña et al. is focused on the application of MD techniques in two-dimensions. The other two studies noted here are experimental in nature, but they do not focus specifically on the solid-fluid transition regime. The present experiments are an expansion of work that we reported earlier [5].

For the present discussion, it is useful to compare the case of a granular material subject to horizontal shaking to the corresponding case of an ordinary block that rides on an oscillating substrate and experiences SoS Coulomb friction. This model is then germane to the case of granular failure along a horizontal plane. For low substrate accelerations, such a block experiences a frictional force F_f of magnitude $|F_f| \leq \mu_s mg$ when the block and the substrate are moving at the same speed. Here, μ_s is the static friction coefficient. The point of Mohr-Coulomb failure in a granular material is analogous to the point at which the SoS friction is inadequate to hold the block on the surface without slipping. If the block and substrate are in relative motion, the friction is reduced, and the frictional force has a magnitude $\mu_k mg$ that is oriented in the direction of $\vec{v}_{substrate} - \vec{v}_{block}$. If the magnitude of the substrate acceleration exceeds $\mu_k g$, then the block necessarily slips. This primitive model shares at least two features with its granular counterpart: first, both exhibit frictional failure when the acceleration exceeds μg, and in both cases, once failure has occurred, we expect that the frictional drag exerted by the substrate will be reduced. There are also important differences between the block and granular systems, and an understanding of these differences is crucial to an understanding of the collective behavior of granular systems. In Section VI, we explore an improved model that captures features that appear in the granular case, but that are not necessarily present in the block-slider case.

The rest of this work is structured as follows. In Section II, we provide details of the experiment and procedure. In Section III, we present a detailed probing of the transition to sloshing flow, and its origins. In Section IV, we consider a number of approaches where we modify the ordinary conditions of the experiment in order to gain insight into the nature of the transition and resulting flow. We use MD studies to probe aspects of the convective flow, as described in Section V. In Section VI, we propose and investigate a simple friction model that accounts for

the hysteresis seen at the transition. Section VII contains a discussion of the results and conclusions.

II. EXPERIMENT

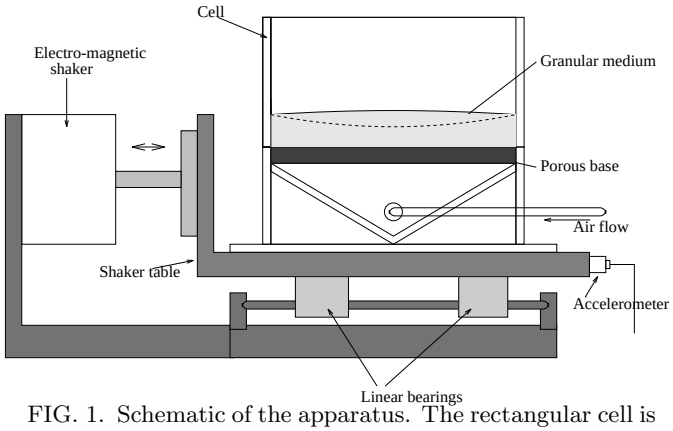

FIG. 1. Schematic of the apparatus. The rectangular cell is made of Plexiglas, and is mounted on a Plexiglas base of the same cross-sectional dimensions. The base is attached to a small table, which in turn is mounted on four linear bearings running on horizontal cylindrical guide rods rigidly attached to a fixed bottom frame. The porous base of the cell can act as a gas distributor. An electro-mechanical actuator, driven by a sinusoidal AC signal provides the horizontal driving.

Our experimental setup is shown in Fig. 1. To facilitate the discussion, we refer to the direction of shaking as x, the horizontal direction perpendicular to x as z, and the vertical direction as y. The heart of the experiment is a rectangular Plexiglas cell with dimensions $L_z = 1.93\,cm$ by $L_x = 12.1\,\mathrm{cm}$. The height, $L_y \simeq 12\,\mathrm{cm}$, of the cell is much taller than the fill height. The base of the cell is made of porous polypropylene (average pore size $50\,\mu m$) through which gas can flow in order to fluidize the granular medium. This provides an independent control over the dilation of the material. The pressure gradient across the distributor is more than 50% of the total pressure gradient; hence, when gas flow is used, there is reasonably even air distribution across the granular bed. The cell is mounted on a Plexiglas base of the same cross-sectional dimensions as the cell, which is in turn mounted on a movable table. The base acts as the gas distributor to the system, and it is connected to a constant pressure source through a flexible hose. The table is mounted on four linear bearings sliding on two horizontal shafts rigidly attached to the fixed bottom frame. An electro-mechanical actuator provides a sinusoidal drive of the form $x = A\sin\omega t$ at frequencies, $f = \omega/2\pi$, spanning $3 - 15\,Hz$ and at amplitudes A, spanning $0 - 15\,mm$. The maximum acceleration that we can achieve with the present apparatus is $\Gamma_{max} \simeq 2$. A calibrated accelerometer [12] mounted on the moving table measures the acceleration of the cell.

In order to investigate the behavior of this system near the relevant transitions points, it is crucial to have a precise measure of Γ. The acceleration is measured with a resolution of $\sim 0.011\%$ with lock-in detection and a bridge circuit sketched in Fig. 2. We discuss the details of the detection process in that figure.

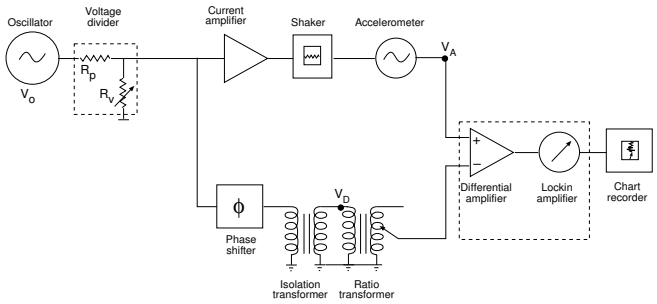

FIG. 2. Schematic of acceleration measurement electronics. The principle of operation is that an oscillator provides a reference source to both a power amplifier and to a ratio transformer (variable center-tapped inductor). The output of the power amplifier drives the shaker. An accelerometer rides with the shaker, and the output of the accelerometer V_A is compared with a fraction of the voltage from the oscillator V_D through a differential amplifier and lock-in detector. This latter voltage has been phase shifted appropriately, so that its phase matches that of the signal from the accelerometer. The bridge circuit is nulled by adjusting the ratio transformer, whose value directly yields the acceleration amplitude.

We note that other parameters besides Γ, might be important, as is the case in describing higher order phenomena in vertically shaken materials (e.g. traveling waves [13] and coarsening [14]). In horizontal shaking experiments, frictional properties are relevant. Recent experiments [9] show that the ratio A/d may be important for highly monodisperse grains which can lock into a crystalline state, depending on that ratio. However, the materials used here were not particularly monodisperse. And, we did not observe any dependence of the qualitative flow properties or of the quantitative results for critical parameters on A/d. We consider this point in more detail below.

We used several types of approximately monodisperse granular materials, including spherical glass beads, smooth Ottawa sand, and sieved rough sand—with similar effects. Some relevant information is summarized in Table I.

Ottawa sand:	average particle diameter 0.6 mm
Rough sand:	average particle diameter 0.6 mm
Glass spheres:	particle diameters $0.2 \leq 2.0\,\mathrm{mm}$
Cell size:	12.1×1.93 cm
Cell depth:	12 cm (≈ 200 grains)

TABLE I. Summary of materials used and of cell dimensions.

Throughout these experiments, we used the following procedure. The material was poured into the cell and partially compacted by flattening the surface. The compaction was enhanced by shaking at relatively low Γ before proceeding to higher values. Typically, the layer had a height $h/d \simeq 40$; as long as $h/d \simeq 20$, we found no dependence on h, as demonstrated below. In a typical run, we observed the evolution of the system as A, and hence Γ, was increased from zero while keeping ω fixed. Once flow was well initiated, we then decreased A.

III. THE PRIMARY BIFURCATION

In this section, we present detailed studies of the experimentally determined bifurcation diagram near onset. We also discuss the character of the flow field in the fluid state. We conclude this section with an exploration of unstable states and a comparison to previous results.

A. A Backwards Bifurcation

As Γ is increased slowly from a low value, the system, regardless of material type, undergoes a hysteretic, i.e. backward, bifurcation at Γ_{cu} to a flow state characterized by strong sloshing motion of a fluidized layer. A useful measure of the strength of the flow is the thickness, H, of the liquefied material in the middle ($L_x/2$) of the cell, as in Fig. 3. We show results for three different materials in Fig. 4. Specifically, with increasing Γ, the solid layer becomes unstable at Γ_{cu} to the formation of a fluidized layer. In the experiments, H was measured by following the motion of the grains using close-up images from a shaker mounted camera. Grain displacements near $x = L_x/2$ decrease roughly linearly with the distance y from the top surface, except for the last few particle layers that separate the fluid and solid. Once the fluid state has formed, it is stable for decreasing Γ until $\Gamma_{cd} < \Gamma_{cu}$. At Γ_{cd}, the fluidized layer disappears, and the material is once more in the solid state. In addition to the sloshing flow, there are two types of circulating or convective flow. The two different convective components have very different origins, and we discuss these below. An additional feature is the existence of a small number of free grains, 'sliders', that move on the surface at Γ's less than Γ_{cu}.

It is interesting that this transition is hysteretic. By contrast, ordinary SoS friction for a block on an oscillating substrate is not hysteretic. Specifically, for the block system, if Γ exceeds μ_s by a small amount, stick-slip motion evolves, in which the block spends part of each cycle slipping, and part moving with the substrate. We discuss this at some length in the context of Section VI and Fig. 24. If Γ is reduced below μ_s, this stick-slip motion vanishes. The important difference appears to be that for the granular system, the grains must dilate in order to flow [15], but once dilated, the flow is more easily sustained. The time needed for this dilation/compaction to occur is an important piece of the explanation for hysteresis in the granular system.

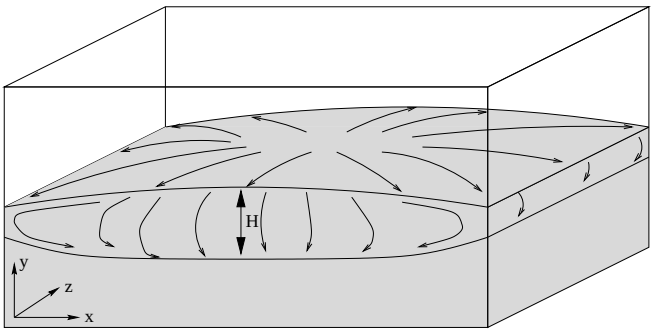

FIG. 3. Sketch of time-averaged convection flow lines in the liquefied layer induced by horizontal shaking as seen in perspective from the top, and side. Grains rise in the middle of the cell, flow along the surface towards the side walls, and then sink at the wall boundaries. Superposed on this motion is the sloshing that occurs in the x-direction.

B. Properties of the Transition

Different ω's or A's yield the same critical Γ_{cd}'s and Γ_{cu}'s for a given material and fill height for the full range of A's and ω's that we explored. Thus, Γ is the relevant control parameter. We document this point in Fig 5, which shows data for Γ_{cu} as a function of shaker frequency. Within experimental resolution (and within the experimentally accessible range of parameters), there is no variation of these Γ's with ω. A similar conclusion follows concerning the independence of critical Γ's on the amplitude, A.

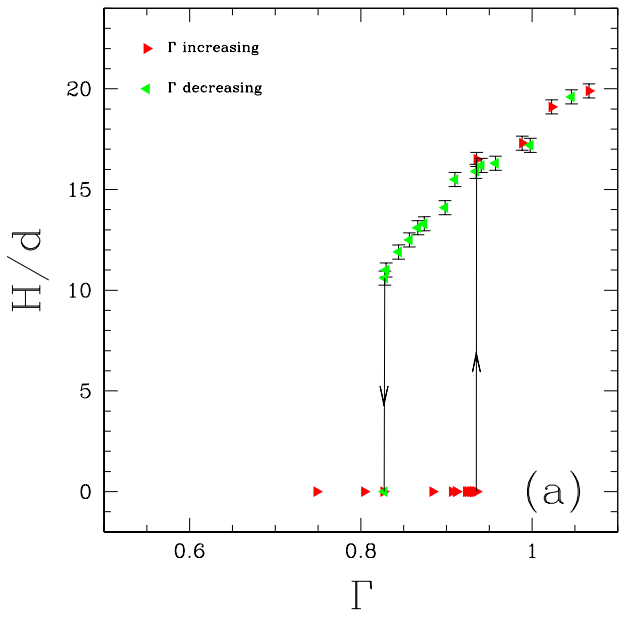

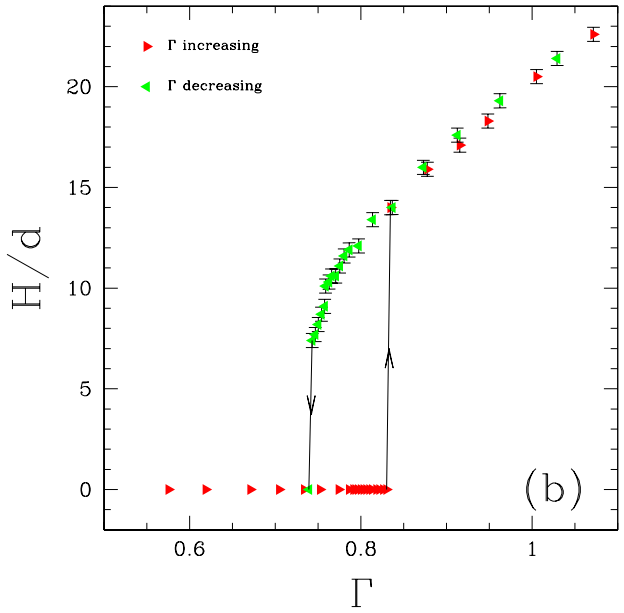

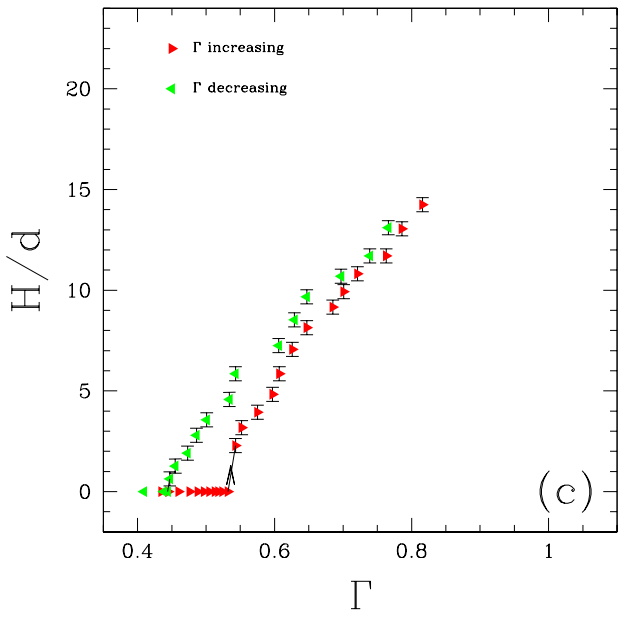

FIG. 4. Bifurcation diagrams for the initial sloshing transition for (a) rough sand, (b) smooth Ottawa sand, and (c) glass beads. The arrows indicate the transition points, $\Gamma_{c[u,d]}$. The transition points and the sizes of the hysteresis loops tend to increase with increasing material roughness. See also Table II.

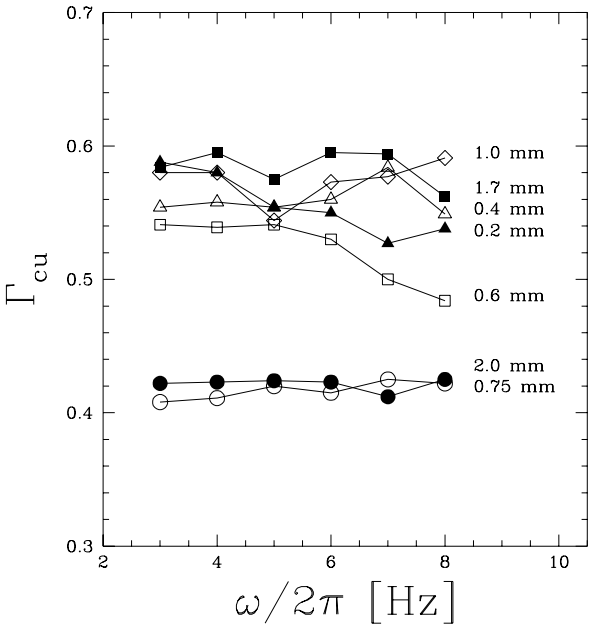

FIG. 5. Values of Γ_{cu} vs. shaking frequency, $f = \omega/2\pi$ for the indicated particles sizes. Here, the particles are glass spheres, and the numbers give the sphere diameters. Within experimental error, there is no systematic dependence on frequency (hence amplitude, A) for the initial transition.

Also of interest is the dependence of this transition on the total depth of the original solid layer before shaking. In Fig. 6 we consider this issue for Ottawa sand. The

transition Γ's, $\Gamma_{c[u,d]}$, are roughly linear functions of the total layer thickness up to a depth of ~ 15 grains. Above this, the critical Γ's cease to depend on the overall thickness of the layer. Since the depth of the fluidized layer that forms at Γ_{cu}, Fig. 4, is $H/d \simeq 14$, we conclude that the system dynamics are unaffected by the total depth of the layer, so long as there is enough material to support the fluidized portion. However, we are unaware of predictions for the thickness of this layer.

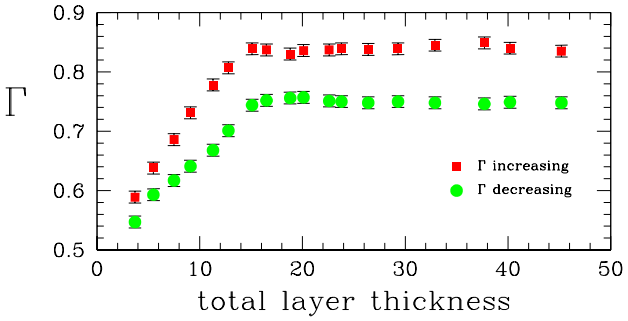

FIG. 6. $\Gamma_{c[u,d]}$ as a function of the total depth of material in the cell, for Ottawa sand. The total depth is scaled by one particle diameter. Above about 15 particle diameters there is no dependence of $\Gamma_{c[u,d]}$ on thickness.

The results for $\Gamma_{c[u,d]}$ do depend on the physical properties of the material, as shown in Fig. 4 and in Table II. For instance, Γ_{cd} and Γ_{cu} increase as the roughness of the granular materials increases. The same is true for the difference $(\Gamma_{cu} - \Gamma_{cd})$, which is larger for rougher materials than for smoother ones. This can be attributed to two factors: first, the ability of rough grains to roll is reduced because of the interlocking of grains; and second, the SoS frictional forces between grains and between grains and walls may also be higher for rough grains.

	Γ_{cu}	Γ_{cd}	$\Delta\Gamma$
rough sand	0.9350	0.8275	0.1075
smooth sand	0.8324	0.7413	0.0911
glass beads	0.510	0.446	0.064

TABLE II. Forward and backward transition points and the size of the hysteresis loop ($\Delta\Gamma = \Gamma_{cu} - \Gamma_{cd}$) for several granular materials. The transition points and hysteresis loop tend to increase with increasing material roughness.

C. Flow in the Liquefied Layer

The flow at the initial instability consists of a sloshing of the grains in the direction of the shaking, plus slower convective flow. Figure 3 shows a sketch of convective flow lines observed from the top and side for Γ somewhat above Γ_{cu} in a layer that is 50 grains deep. In Fig. 7, we show a specific image of the particle flow for half of the cell, as seen from above. We obtained this image by coloring some of the particles and by then following them over time to generate a streak photograph. (In this regard, considerable care must be taken with the coloring, since coloring can affect the surface friction, leading in turn to segregation.) Grains rise up in the inner part of the cell, flow along the free surface towards the side walls, and then sink at the wall boundaries. In this circulating flow, there is a component along the direction of shaking, and in addition, a component transverse to this direction. The top surface of the liquefied layer has a dome shape which is concave down, and the bottom surface of this layer is concave upwards near the wall boundaries. The thickness of the fluidized layer is largest in the middle of the cell and smallest at the end walls, as seen previously [8]. In the case of thin cells, where the widths of the cells are less than six grain diameters, the convective flow transverse to the shaking direction is suppressed and the curvature of the top surface perpendicular to the motion direction vanishes. As Γ is decreased from above towards Γ_{cd}, grains near the end walls ($y - z$ planes) stop moving first, while grains in the middle keep moving. The convective flow in the transverse direction is analyzed by additional experiments and also by molecular dynamics simulations in Section V.

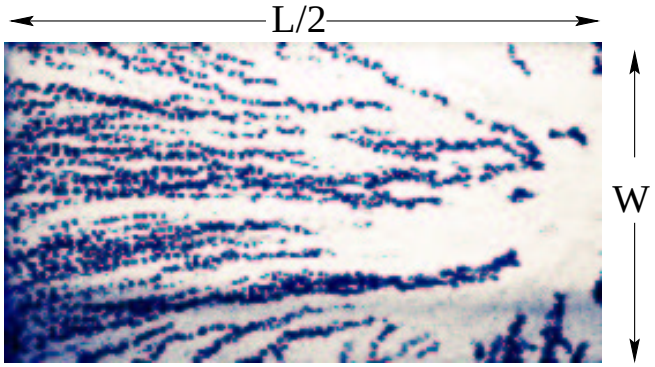

FIG. 7. Image of the left half of the top of the container, showing the two directions of convective flow. This image was generated by coloring some of the grains and by then superposing a series of images to produce an effective streak image.

D. The Unstable Branch

The hysteretic character of the transition to fluidization suggests that there is a separatrix in (H/d)–Γ space

connecting the fluid state at Γ_{cd} with the solid state at Γ_{cu}. If a perturbation of size h is created for $\Gamma_{cd} \leq \Gamma \leq \Gamma_{cu}$, this perturbation will grow to the fluid state if h lies above the separatrix, and it will shrink if it lies below. (In the case of a simple backwards bifurcation, this curve is a line of unstable equilibrium states.) Such a curve does exist for this system, and we have accessed it by applying controlled perturbations consisting of small bursts of pressurized air. We use the device sketched in Fig. 8. A constant pressure air flow jets onto the granular surface. A solenoid valve controls the jet duration, which in these experiments was fixed at 1 sec. The jet deposits a fixed amount of momentum to the surface, which we adjust by changing the pressure. Note that the perturbation could produce different results if the jet were directed at an angle to the surface. However, in these experiments the jet always impinged perpendicularly to the surface. The resulting bolus of air is delivered to a region directly above the middle of the surface of the granular material through a flexible tube that is terminated by a glass eye-dropper. Depending on the value of Γ, there is a well defined and reproducible pressure pulse that is just sufficient to initiate a transition to the fluid state if $\Gamma_{cd} \leq \Gamma \leq \Gamma_{cu}$. Just above Γ_{cd}, a modestly large pressure pulse is needed to make the transition to the fluidized state; just below Γ_{cu}, only a tiny pulse is needed. We show the locus of this curve, along with the data for H/d for the case of smooth Ottawa sand in Fig. 9. Here, we have rescaled the pressure pulse data so that it coincides with the curve of H/d at Γ_{cd}. A useful feature of this procedure is a demonstration of the fact that the system is unstable to very weak perturbations as Γ approaches Γ_{cu} from below. For instance, Fig. 10 shows the amount of excess pressure needed to initiate the instability and the time interval from application of the pulse to a completely sloshing cell.

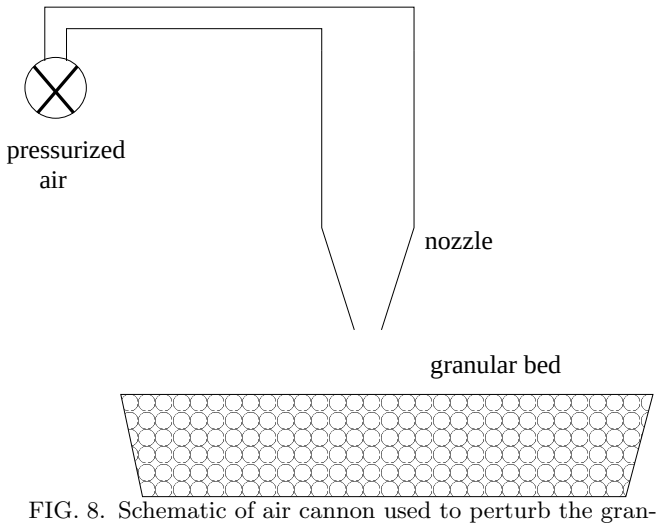

FIG. 8. Schematic of air cannon used to perturb the granular surface.

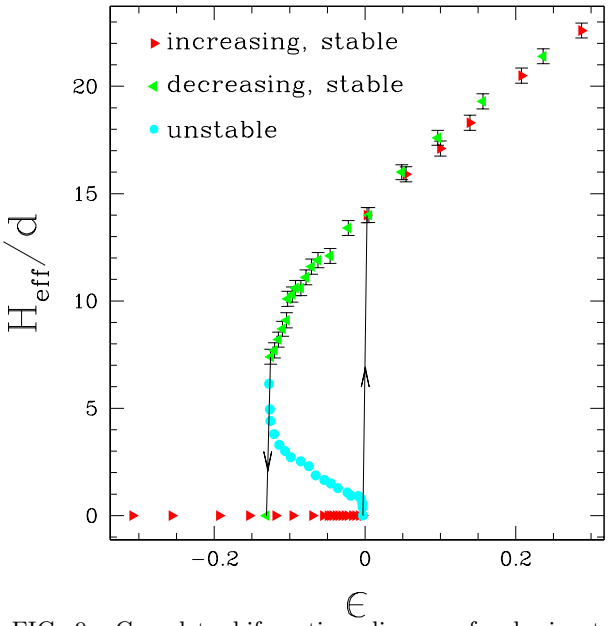

FIG. 9. Complete bifurcation diagram for horizontally shaken smooth Ottawa sand.

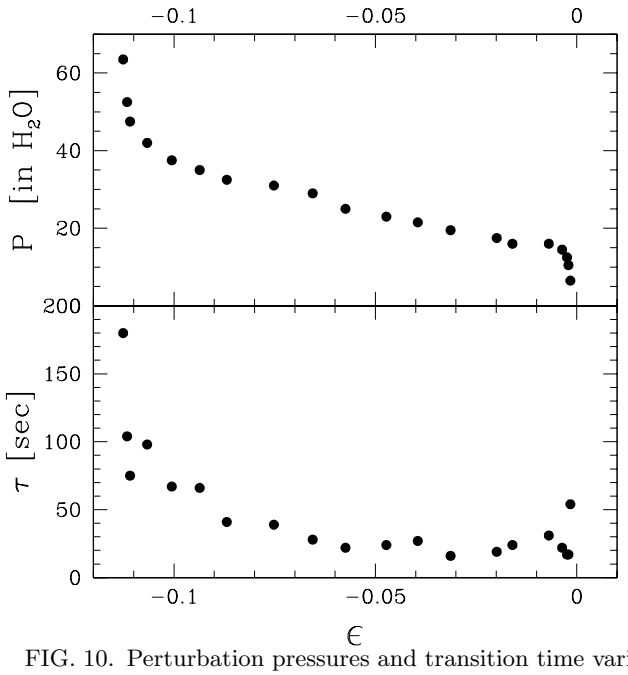

FIG. 10. Perturbation pressures and transition time varies along the unstable branch of figure 9. Plotted above is the perturbation in pressure units of inches of water. Plotted below is the time interval from application of the perturbation to completion of the transition versus $\epsilon = (\Gamma - \Gamma_{cu})/\Gamma_{cu}$.

E. Nucleation of the Fluid State and Decay to the Solid State

The spatial character of the onset to flow is an important aspect of the transition from solid to fluid with

increasing Γ, and the parallel transition from fluid to solid with decreasing Γ. We consider first the case of increasing Γ, starting in the solid state. In this case, the solid becomes unstable via a local perturbation. Fig. 11 is a space-time plot that shows the horizontal extent of the fluidized region in white. Time starts at the top of the figure and evolves downward. Each horizontal line is digitized from 30 frame/sec video and spans the entire cell width. Total time in the figure is 18.4 seconds. The initial location of this 'nucleation' of sloshing occurred with an approximately uniform probability anywhere in the cell except for a 5 or 6 particle wide zone next to each end wall. The nucleation consists of a local dilation/fluidization of the upper surface of the layer. This perturbation remains localized until it has penetrated relatively deeply, and only then spreads to the whole layer. This scenario is surprising in light of the usual Mohr-Coulomb failure picture where we expect that the material would fail along a nearly planar surface, starting from the top of the layer where the normal stresses from gravity are least.

The time needed for a perturbation to nucleate is particularly interesting. If the system is equilibrated at $\Gamma < \Gamma_{cu}$, and then Γ is increased past Γ_{cu} by an amount $\epsilon\Gamma_{cu} \equiv (\Gamma - \Gamma_{cu})$, the time to nucleate a defect diverges as $\tau_u = \tau^* \epsilon^{-\beta}$, where $\beta = 1.00 \pm 0.06$ is indistinguishable from unity. We document this in Figs. 12 and 13 for Ottawa and rough sand respectively. After nucleation, the time for sloshing to spread to the whole cell is roughly constant (8–15 sec) for our cell and independent of ϵ.

The time for the fluidized material to vanish when Γ is decreased below Γ_{cd} by $\epsilon\Gamma_{cd} \equiv (\Gamma - \Gamma_{cd})$ is equally striking: this time, τ_d, follows a power law indistinguishable experimentally from that for τ_u. Specifically, if Γ is stepped below Γ_{cd} by a very small amount, the fluidized material vanishes over a long transient, as typified by Fig. 14.

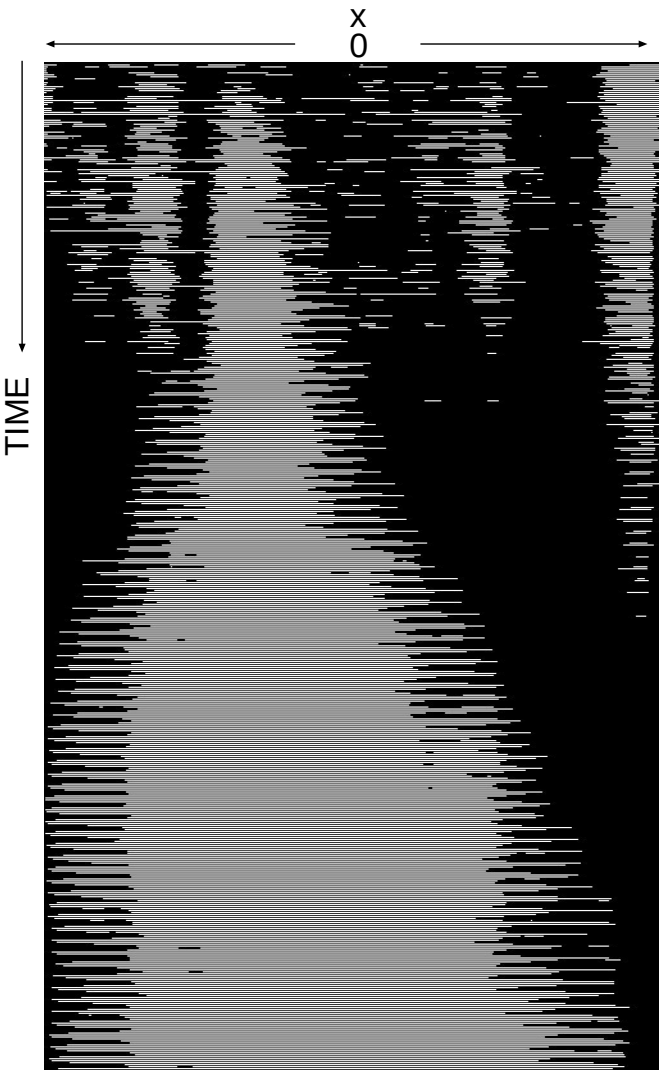

FIG. 11. Space-time plot showing the nucleation and growth of the fluidized region in Ottawa sand. Here, time runs top to bottom, and we show the horizontal extent of the fluidized region of the layer in white. The figure spans the entire width of the experimental cell and covers 18.4 sec at 0.033 sec per line.

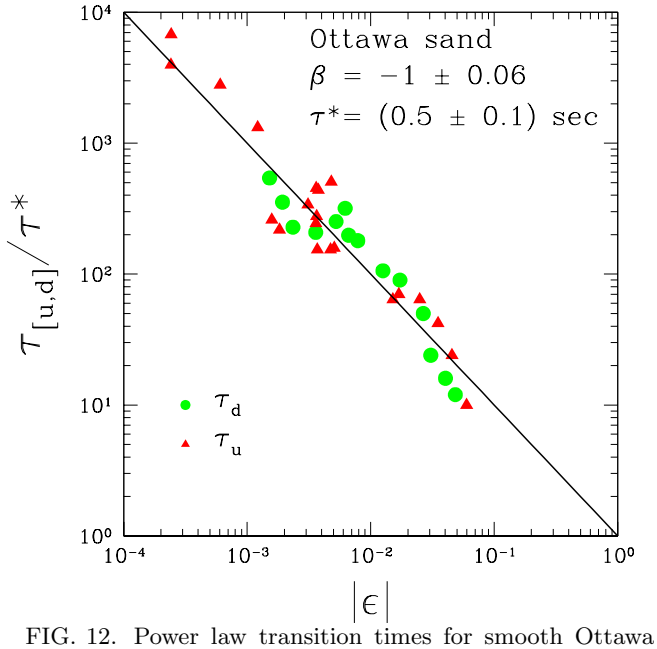

FIG. 12. Power law transition times for smooth Ottawa sand. The circles are for the transition from fluid to solid, and the triangles are for the transition from all solid to the state with a fluid layer.

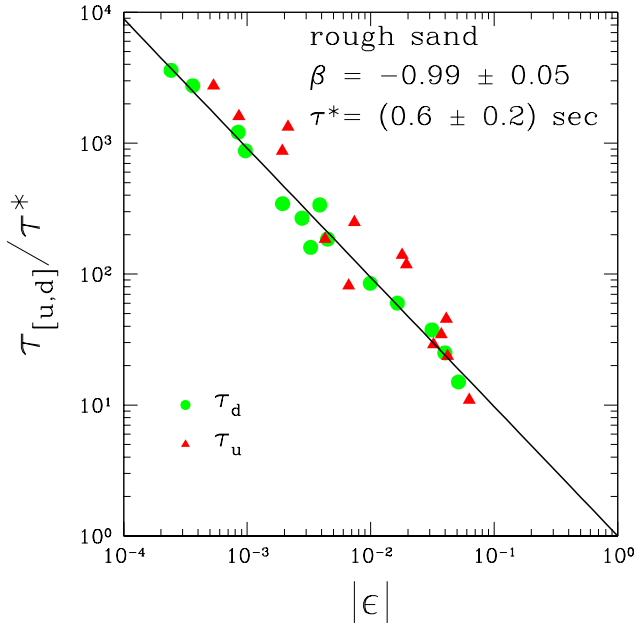

FIG. 13. Powerlaw transition times for rough sand. The symbols are the same as those for Ottawa sand.

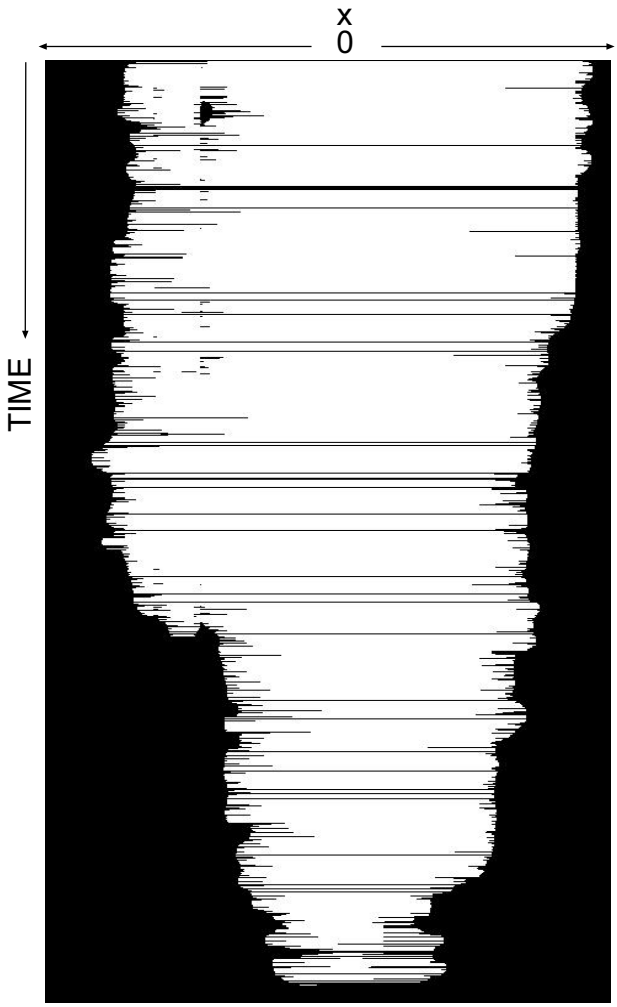

FIG. 14. Space-time plot showing the vanishing of the fluid layer for a small step below Γ_{cd} in Ottawa sand, similar to figure 11 for nucleation growth but covering a total time of 919 sec at 1 sec per line.

F. Comparison to Other Work

It is useful to compare our observations to previous MD calculations and experiments. Regarding hysteresis, we note that some hysteresis is present in 2D studies by Ristow et al. [11], but the hysteresis in our 3D experiments is larger, particularly for rougher materials. Also, we do not see the 4-roll state reported by Liffman et al. in 2D MD studies [10]. In order to further pursue their prediction, we have tried to replicate these studies [10] using a tall narrow cell for which L_x is similar to the model value (30 particle diameters), and L_z is only slightly larger than a particle diameter. However, we still do not observe the secondary 4-roll convective state for $\Gamma \leq 2$. We note that 4-roll states have been experimentally observed by Medved et al. [6] but in a 3D system, at much larger ac-

celerations, and with an opposite sense of rotation from those predicted in [10] (see also [7]). It seems most likely that friction with the sidewalls significantly perturbs the experimental flow, thus limiting the similarity between the system considered here and in [10]. Also using MD, Zhang and Campbell [21] study the solid to fluid (but not the reverse) transition. They find the transition follows a Mohr-Coulomb failure mode with a flow rapidly changing from stagnant, through quasi-static to fully mobilized rapid granular flow.

IV. MODIFYING THE BIFURCATION

In order to obtain additional insight into the collective process that is at play in the fluidization and transition processes, we have carried out several additional experiments (without the gas puffer) that modify the conditions of the layer. Interestingly, even seemingly weak perturbations have a dramatic effect on the transition. The modifications to the unperturbed flow that we consider here include a) vertical gas flow (below the fluidization pressure), b) suppression of the sliders by a light, solid strip of plastic; and c) the addition of a particle on the surface that is more massive than the sand particles. We discuss these experiments and their results in the following subsections.

A. Air Fluidization

To obtain additional insight into the relative importance of dilatancy and friction, we have fluidized the granular bed by passing air through it, using the flow-controlled air supply and the porous base of the shaker (see Fig. 1). Here, the goal is to remove or reduce the interlocking of the grains. Figure 15, which presents Γ_{cu} and Γ_{cd} as a function of the measured pressure difference ΔP across the granular medium, indicates a strong dependence of these quantities on dilation. In this figure, we nondimensionlize ΔP by the weight W of the granular material per unit area. In particular, a modest air flow corresponding to about 40% of the weight of the bed reduces the critical Γ's by as much as half, and effectively removes the hysteresis in the initial transition. The measured dilation of the bed at this point due to the air flow corresponds to less than one granular layer for a bed of 45 layers, i.e. less than 2% dilation. As a rough comparison, all interlocking is removed for a square sphere packing (solids fraction $\nu = 0.52$), whereas a typical dense sphere packing has $\nu = 0.64$; these differ by 18%.

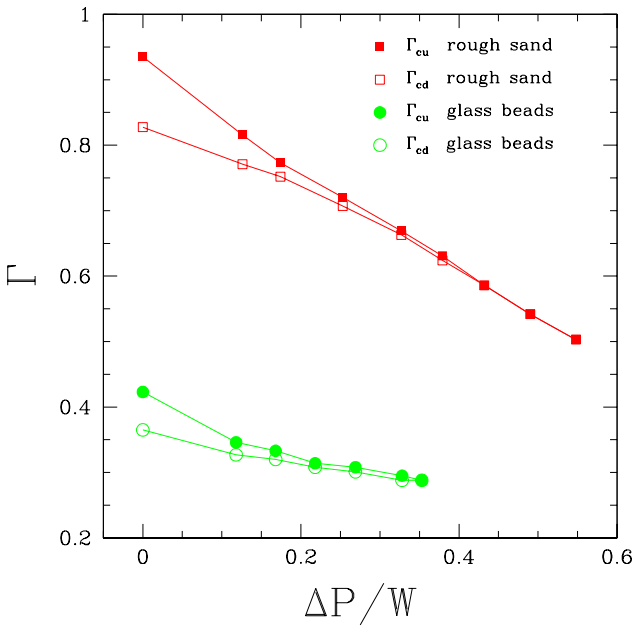

FIG. 15. Modification of bifurcation points, $\Gamma_{c[u,d]}$, by air fluidization for smooth Ottawa sand. ΔP is the pressure difference across the granular material normalized by its weight per area, W.

B. Effect of a Uniform Overburden

The Mohr-Coulomb picture of failure suggests that the transition from solid to fluid would occur along a roughly planar surface such that the material is at the failure locus. The end walls provide additional stress, so that the failure locus need not be exactly planar. However, in these experiments, the failure occurs at a local nucleation site.

In order to further investigate the issue of what causes failure, we added an overburden consisting of strips of plastic that covered the majority of the upper surface of the sample. These strips were free to move vertically and also had limited (less than half a particle diameter) freedom of movement in the horizontal directions. The expectation was that this overburden would apply an additional uniform force on the sample, hence elevating the transition point, and possibly increasing the amount of hysteresis in the bifurcation diagram, H-vs-Γ.

Neither of these expectations were borne out in the experiment. Rather, the transition point from solid to fluid occurred at a value of Γ that was slightly less than Γ_{cd}, and no hysteresis was evident. We document this in Fig. 16. Here, the open symbols represent the original data obtained without any overburden, and the solid symbols represent the data obtained with an overburden that has a mass corresponding to 0.5 grain layers–a very slight overburden. With this overburden, there is now a jump in the mean thickness of the layer at the transition, and no observable hysteresis.

The behavior with the overburden is what we would expect from a naive friction model with an instantaneous change between μ_s and μ_k. The low mass of the overburden suggests, in the context of the Mohr-Coulomb picture, that it should have a relatively weak affect on the granular failure. Yet, it has a dramatic effect on the transition. The overburden strips play at least one clear role on the dyanamics of this system, which is to suppress the layer of 'sliders', i.e. the small number of free gas-like particles that are present for Γ's below Γ_{cu}. In general, however, we can only speculate on the mechanism that changes the bifurcation. One possibility is that the suppression of the sliders and the additional small overburden makes the system more uniform. Alternatively, the sliders may stabilize the surface layer by strengthening weak regions or by disrupting the growth of an unstable nucleus.

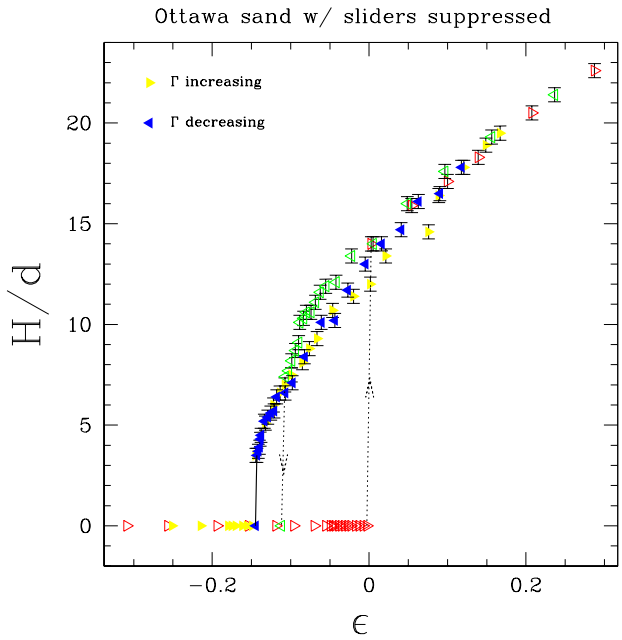

FIG. 16. Modification of the bifurcation by a small overburden, for smooth Ottawa sand. In this case, the mass of the overburden corresponds to 50% of one layer of particles. The primary physical effect of the overburden appears to be a suppression of the motion of the surface "sliders". Open symbols and dotted lines are the scaled data with no suppression from figure 4(b). Filled symbols are the data with slider suppression. The hysteresis loop disappears, and the bifurcation appears similar to that expected for a Coulomb block, c.f. Fig. 24*a*.

As the amount of confining pressure, P_c, from an overburden increases, the depth of the fluid layer is systematically reduced. We show this is Fig. 17. Here, we normalize P_c by the mass per area of a single layer of grains. The different symbols show different initial H/d's (and hence Γ's) corresponding to unburdened layers from figure 4b. For small overburdens, there is a linear reduction in H as P_c is increased. As P_c increases, H/d tends to asymptote to a minimum value of $H/d \simeq 5$, regardless of the thickness that the layer would have in the absence of an overburden. The figure inset shows the slope of the solid lines as a function of the unburdened layer height. The deeper the initial fluidized layer (or the larger Γ), the fewer layers cease sloshing on application of greater confining pressure.

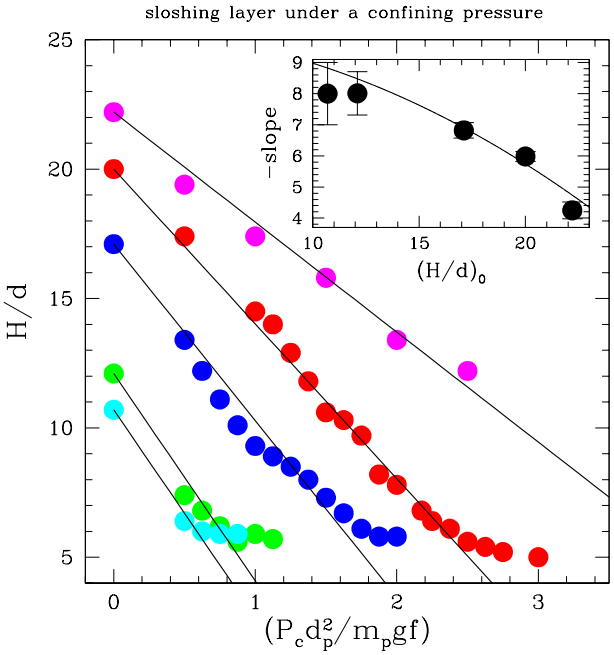

FIG. 17. Depth of sloshing layer of smooth Ottawa sand as a function of confining pressure, P_c, at several unconfined layer thicknesses. The confining pressure is scaled by the weight of one layer of particles. m_p and d_p are a particle mass and diameter. f describes the layer packing fraction, assumed to be 0.64, which is appropriate for random close packing.

C. Surface Impurities

The addition of an impurity particle that is larger or more massive than the rest of the particles in an approximately monodisperse sample has a strong effect on the relaxation time from the fluid to the solid when Γ is decreased below Γ_{cd}. By adding a much more massive particle, it is possible to sustain the fluid phase for times that are four orders of magnitude greater than in the absence of the intruder. In particular, the exponent β can be increased in magnitude from 1 to ≈ 3. Fig. 18 shows relaxation times vs. ϵ for various particles in Ottawa sand, which has a typical grain diameter of 0.6 mm. The dotted line is the least-squares fit to the unperturbed data. Note that the exponent, β in the power law $\tau \propto |\epsilon|^{-\beta}$ rises dramatically. In Fig. 19, we show that it is the mass of the intruder that is responsible for the change in β. Specifically, when we plot β versus the intruder

diameter, density and mass (relative to a sand particle), we find that only in the last case is there a consistent functional relation, i.e. a simple quadratic relation.

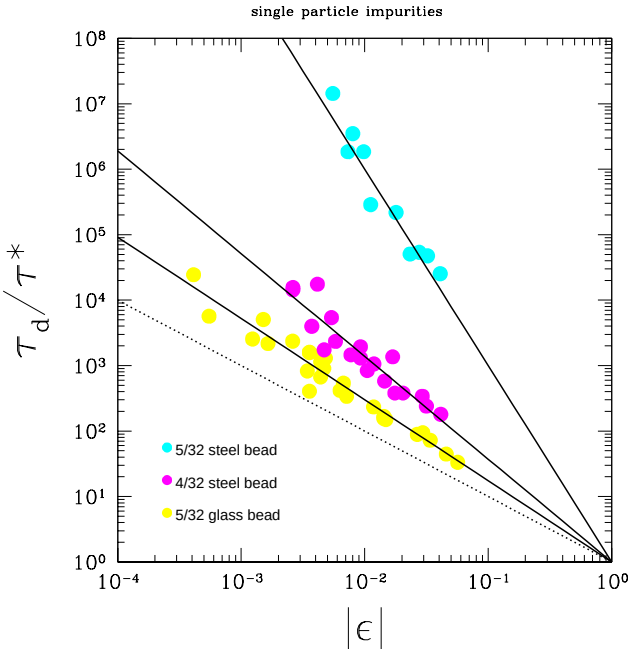

FIG. 18. Modification of down transition times by a *single* particle impurity in smooth Ottawa sand The impurity particles were standard steel or glass spheres, whose diameters are indicated in the figure.

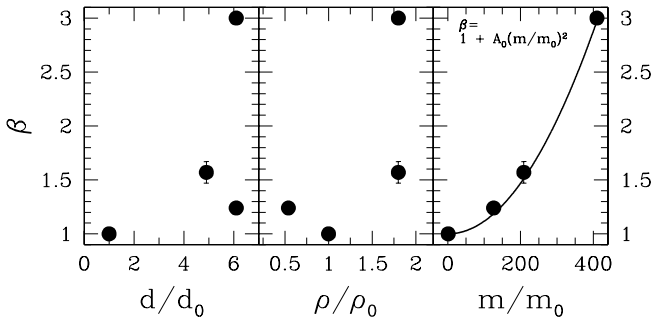

FIG. 19. The power law exponent β for sloshing turnoff with a single particle impurity in Ottawa sand has a simple relationship to the ratio of the impurity mass, m, to a sand grain mass $m_\circ$: β is proportional to the square of the mass ratio, with the single fit coefficient $A_\circ = (1.17 \pm 0.02) \times 10^{-5}$. There is no correlation of β to the size ratio or the density ratio.

V. MD PROBE OF THE ORIGINS OF CONVECTIVE FLOW

An important issue concerns the sources or "motors" which drive both the convective flow parallel to the shaker plane and the convective flow perpendicular to it. The back-and-forth sloshing motion is an obvious consequence of the driving. The convective flow parallel to the x direction is due to the avalanching of grains at the end walls during the sloshing motion of the liquefied layer. Each half of the shaker cycle, grains pile up against one end wall $(y-z)$ plane and a gap opens near the opposite end wall. When the opening at the end wall is sufficiently large, grains near the opening avalanche down to fill part of the gap. This process repeats at alternating endwalls every half cycle.

The convective flow in the z direction, i.e. transverse to the shaking direction, is due to a completely different and novel mechanism. At the long sidewalls there is downward flow of material that is caused by shearing of the grains, an accompanying dilation, and gravity. Specifically, the shearing creates small open spaces into which surface grains fall.

To investigate this flow, we have carried out MD simulations as well as additional experiments where we only oscillated one of the long side walls, keeping the rest of the cell fixed. This captured the effect of horizontal shearing, the dilation of the grains there, and the downward flow.

The MD simulations were performed on a 3D system of 7000 spherical particles. Periodic boundary conditions were assumed in the shearing (x) direction, while impermeable walls bounded the system in y and z directions. The container, which has lengths, in particles diameters of $20 \times 20 \times 20$, was mapped to a $(0,1)^3$ computational domain. The results given below were obtained by averaging over 30 periods of the wall motion and were found to be influenced by neither the diameter nor the monodispersity of the particles.

The MD method is outlined in [16], with particle-particle and particle-wall interactions modeled by a commonly used force law which includes interactions in both the normal and tangential directions (see, e.g. [17,18]). More precisely, the normal force between particles i, j is modeled as

$$\mathbf{F}^n_{i,j} = [k(d - r_{i,j}) - \gamma_n \bar{m}(\mathbf{v}_{i,j} \cdot \mathbf{n})]\,\mathbf{n}\ , \qquad (3)$$

and the force in the tangential direction is given by

$$\mathbf{F}^t_{i,j} = min\,(-\gamma_s \bar{m} v_{rel},\ \mu|\mathbf{F}_{i,j} \cdot \mathbf{n}|)\,\mathbf{s}\ . \qquad (4)$$

Here, d is the diameter of a particle; k is the force constant; $r_{i,j} = |\mathbf{r}_{i,j}|$; $\mathbf{r}_{i,j} = \mathbf{r}_i - \mathbf{r}_j$; $\mathbf{n} = |\mathbf{r}_{i,j}|/r_{i,j}$; $\bar{m}$ is the reduced mass; γ_n is the damping constant in the normal direction due to inelasticity of the collisions; $v_{rel} = \mathbf{v}_{i,j} \cdot \mathbf{s}$;

$\mathbf{s}$ is the unit tangent vector specified by the two conditions: $\mathbf{s} \perp \mathbf{n}$, $\mathbf{s}$ in the plane $\mathbf{v}_{i,j}$; γ_s controls tangential damping, and μ is the Coulomb friction coefficient that specifies the ratio between shear and normal stresses. This model neglects rotational degrees of freedom. While this assumption is necessarily a departure from reality, the main influence of the rotations of the particles on the dynamics in this system would most likely be a change of the tangential damping, γ_s. Our simulations with different values of γ_s show that the results are largely insensitive to the value of this parameter.

The simulations are by and large performed with monodisperse particles. Additional simulations performed with polydisperse particles (characterized by the average radius d) led to similar results.

The simulations presented here assume "rough" walls, built from the same spherical particles as in the system, arranged on a regular lattice. The interaction of the system particles with the walls is modeled by a similar force law, modified by the assumption that the walls do not move as a result of the interaction with the particles. While this approach adds to the computational cost [19], the advantage is that it is easy to change the roughness of the wall by changing the separation and the size of the wall particles.

In the simulations, we use values for the parameters that are appropriate to our experiments. The size of particles is $d = 2$ mm, the amplitude of the wall motion is $A = 1.0$ cm, and the frequency is varied between 2 and 5 Hz. The force constant has a value of $k = 4.0 \times 10^4\, mgd^{-1}$, leading to the collision time [17,18] of $\tau \approx \pi\sqrt{\bar{m}/k} \approx 5.0 \times 10^{-5}$ sec. We have verified that this time is short enough that the results are not influenced by the value of k [20]. The computational time step is $\Delta t = \tau/50$, so that there are approximately 5×10^5 computational time steps during one period of the wall motion for $f = 2$ Hz. The damping constant in the normal direction is $\gamma_n = 114.5\,(g/d)^{1/2}$, leading to a coefficient of restitution in this direction of $e_n = 0.82$. Also, we set $\gamma_s = \gamma_n/2$, so that $e_s = e_n$, and $\mu = 0.5$ [17]. While there is considerable freedom in the choice of parameters, we have verified that the results are by and large insensitive to their values.

The first step in the simulations is equilibration under gravity. The particles are distributed on a rectangular lattice, given random initial velocities and left to settle under gravity (during this stage, the walls are static). This part of the equilibration is considered complete when the total velocity of the particles in the up - down direction becomes sufficiently small. At this point, one of the walls starts its prescribed motion given by $x(t) = A\sin(\omega t)$, leading to additional flow of the particles, due to the rearrangement induced by the moving wall (the same effect as if the system were shaken). The data are not taken as long as there is significant average downward motion of the particles due to this settling process. Typically $10 - 20$ periods of the wall motion are needed for this part of the equilibration of the system to be complete.

After the equilibration, we start recording the required variables, in particular the volume fraction and the velocity of the particles. Since the results are subject to significant statistical fluctuations, they are averaged in the following manner. First, the computational domain is split into a number of averaging cells, typically $15 \times 15 \times 15$ (due to the settling of the particles under gravity and the wall motion, some of these cells do not contain particles). Then, we calculate the total velocity and the number density by summing over all the particles whose centers are in a given cell. This averaging is performed every $20,000$ computational time steps (about 25 times per period of the wall motion for $f = 2$ Hz). Additional time and space averaging is performed, depending on the variable in question. For example, the velocity of the particles adjacent to the shearing wall (Fig. 20a) is calculated by space-averaging over all the cells in the $x - y$ plane next to the wall, and then time averaging over the total duration of the simulation. The results presented here are obtained by simulating 30 periods of the shearing wall motion (after the initial 20 cycles used for equilibration), which corresponds to 15 sec of real time (for $f = 2\pi/\omega = 2$ Hz) or to about 1.5×10^7 computational time steps. We have verified that only minor changes of the results occur if the number of averaging cycles is varied in the range 25 - 40.

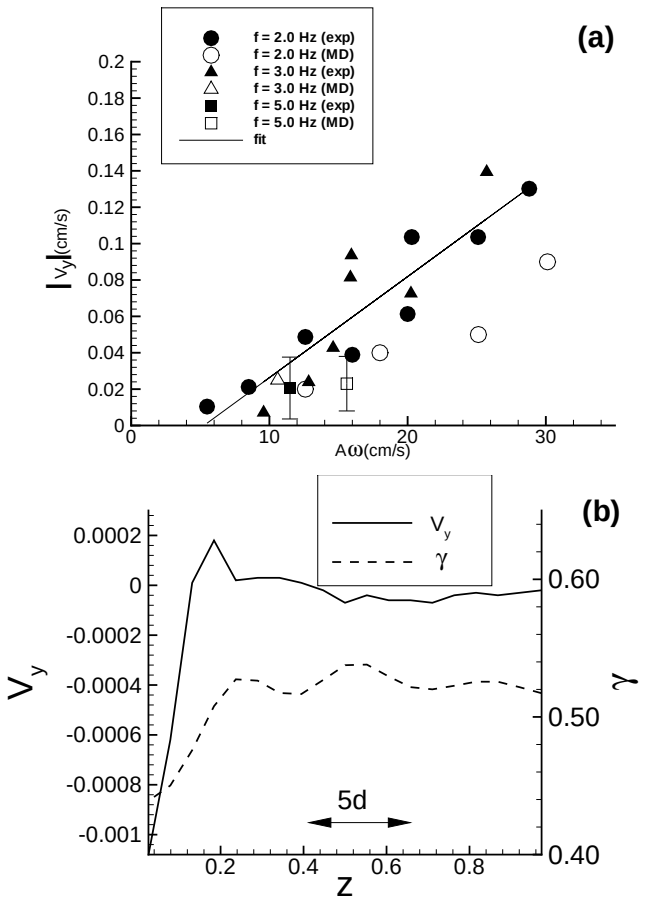

FIG. 20. (a) The average speed at which grains fall along the shearing wall versus shearing speed $A\omega$ of the wall for experiments (solid symbols) and simulations (open symbols). The line is the least square fit to experimental data. The error bars show two typical standard deviations. (b) MD results for V_y (in units of $A\omega$), and for solids fraction γ ($A = 1\,cm, f = 2\,Hz$). An indication of the particle diameter, $d = 2\,mm$, is also shown.

Figure 20a shows the MD and experimental results for the average speed v_y at which the particles fall along the shearing wall, as a function of shearing speed, $A\omega$. We find that V_y varies approximately linearly with $A\omega$. While MD simulations give slightly smaller values for V_y compared to the experiment, the results are consistent up to the experimental and computational accuracy. We have not observed significant changes in the results when the simulations or experiments are performed with particles of different size. Also, the results presented here do not depend in any significant manner on the roughness of the wall in the MD simulations, or on the monodispersity of the particles, even though some ordering of the system particles next to the walls have been observed in the simulations performed with monodisperse particles.

Figure 20b shows the velocity of the particles in the y direction (a '+' sign corresponds to upward motion), and the solid fraction, γ, occupied by the particles, as a function of the horizontal distance from the shearing wall, which is at $z = 0$. There is strong motion of the particles just next to the shearing wall in the $-y$ direction, as well as a pronounced positive peak in the velocity profile at about 2-4 particle diameters in from the wall. Furthermore, the volume fraction is significantly reduced just next to this wall. These two features parallel our experimental observation that the dilation close to the shearing wall allows nearby particles to flow predominantly down. These particles have to move inward, and then develop upward flow in the interior of the shearing layer. In the experiment, the upward flow, presumably occurs deeper in the layer leading to a clear central hump.

The dynamics of the particles strongly depends on the phase of the shearing cycle, as shown in Fig. 21. This figure presents the total momentum of all particles in the x, y, z directions as a function of the phase of the cycle where these results are averaged over 30 cycles. There is a clearly defined harmonic pattern of the motion in the x direction, due to the fact that momentum is being transferred from the shearing wall to the system particles. We observe that the particles move predominantly in the $-y$ direction during those parts of the cycle when the wall velocity changes sign, i.e. whenever the magnitude of the wall acceleration, and hence the shear stress, are the largest. These are the parts of the cycle when significant rearrangement of the system is induced by the wall motion, freeing space for the particles from the upper parts of the system to fall under gravity. During the rest of the cycle, there is predominantly motion in the $+y$ direction, as required by the (approximate) incompressibility of the system. Also, during the parts of the cycle characterized by the large acceleration of the wall, the particles move predominantly away from the shearing wall (positive P_z), while motion towards the wall results during the rest of the cycle. Note that the downward motion ($v_y < 0$) correlates well with the inward motion ($v_z > 0$).

Better insight into this and other effects can be obtained from Fig. 22, which shows the velocity field of the particles in the y and z directions at different phases of the cycle. We immediately observe that the dominant contribution to the dynamics comes from the part of the system that is closest to the shearing wall, with no significant motion away from this wall. One interesting observation is that the motion is considerably stronger in the upper parts of the sample, because the lower part is compacted due to gravity. We observe a similar trend in the experiment for the particles that are next to the shearing wall.

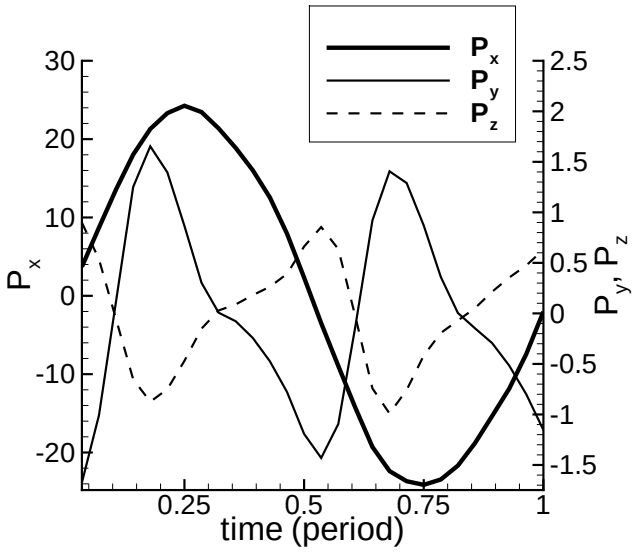

FIG. 21. Total momentum (in arbitrary units) as a function of time during one cycle of wall motion.

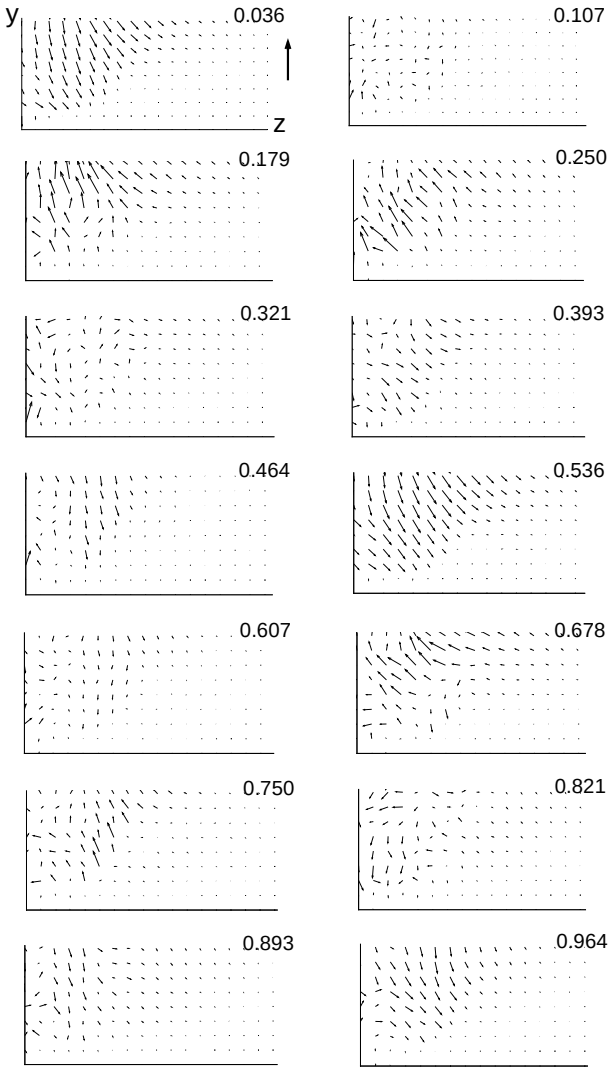

FIG. 22. Velocity of the particles in the y and z directions for the complete cross section of the cell during different phases of the driving cycle (the y and z axes correspond to the shearing and bottom walls, respectively). The numbers on the plots refer to the phase in units of 2π. The velocity vectors are averaged over 30 cycles. The reference vector of length 0.1 in units of $A\omega$ is shown in the first plot ($A = 1.0$ cm, $f = 2$ Hz).

Figure 22 clearly shows different directions of particle motion for different phases of a cycle. For particles that are far from the shearing wall, the motion in the $-y$ and $+z$ alternates direction during a cycle. We conclude that the convection of the particles next to the shearing wall is a net result of two competing regimes during different phases of the driving cycle. As such, the resulting mean flow is relatively weak; the magnitude of the time dependent velocity of the particles during a given part of a cycle can be much larger then the mean convection velocity.

VI. OSCILLATING FRICTIONAL BLOCKS

Before closing, we consider a model that can describe the fluid-solid transition process more accurately that the naive Coulomb friction model discussed in the introduction. The important modification of the Coulomb picture is the incorporation of a relaxational process for the friction coefficient, which in rescaled form, is indicated here as $\theta(t)$. This approach is similar in spirit to the model of Carlson and Batista who considered friction between lubricated surfaces [22]. The addition of this feature leads to a somewhat more realistic description of the collective dynamics, and in particular, the resulting model correctly predicts a backward bifurcation.

In the new model, we still assume that the material that is to become fluid is represented by a frictional block on an oscillating surface. The equations of motion of the frictional block include an evolution term for θ, as well as the acceleration, $\dot{y}$, where y is the block velocity relative to a substrate. The substrate has a velocity $v = A\cos(\omega t)$, as schematized by the top of Fig. 23. In the analysis below, we use $2\pi/\omega$ as a time scale, and we normalize so that the friction coefficient has a maximum value $\theta = 1$. (Thus, ω does not appear in the expressions below.) The frictional force f on the block is now characterized by a time-dependent friction coefficient, θ:

$$\begin{array}{ll} y \neq 0 & \{\ f = -\theta \mathrm{sign(y)} \\ y = 0 & \begin{cases} f = -A\sin(t) & \text{if } |A\sin(t)| < \theta \\ f = -\mathrm{sign}(\sin(\mathrm{t}))\theta & \text{if } |A\sin(t)| \geq \theta \end{cases} \end{array} \qquad (5)$$

In the sliding regime, $\dot{y} \neq 0$, we introduce the following evolution equation for θ that supplements the force law:

$$\dot{y} = f + A\sin(t) \tag{6}$$

$$\sigma\dot{\theta} = 1 - \theta\left(1 + R\frac{|y|}{W + |y|}.\right) \tag{7}$$

The equation for $\dot{\theta}$ is structured so that when y vanishes, $\theta \to 1(= \mu_s)$. And, if $y \neq 0$, θ will decrease to $1/(1 + R) = \mu_k$. The term multiplying R is chosen so that θ saturates at μ_k when the velocity exceeds the small threshold value W. The key new feature is that the frictional force evolves towards its static or dynamic values with a time constant σ. The Coulomb case of instantaneous switching between static and dynamic friction is a singular case of the limit $W \to 0$, $\sigma \to 0$. We note that in order to model the Coulomb case numerically, we explicitly set $\theta = 1$ whenever $y = 0$, in which case $\dot{\theta} = -R/\sigma$ is large and negative for σ small. In turn, this causes a quick change from $\theta = 1$ to $\theta = \mu_k$ when $y \neq 0$. We contrast the switching of the frictional force for the simple Coulomb and relaxational models in the lower part of Fig. 23.

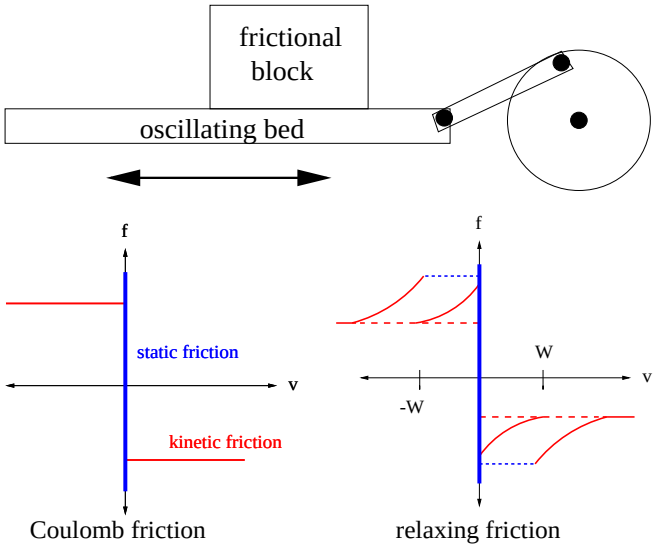

FIG. 23. (top) A sketch of the heuristic block model. (bottom) The relaxation processes for simple Coulomb friction, and the modified model. The latter incorporates a relaxation process between static and dynamic friction.

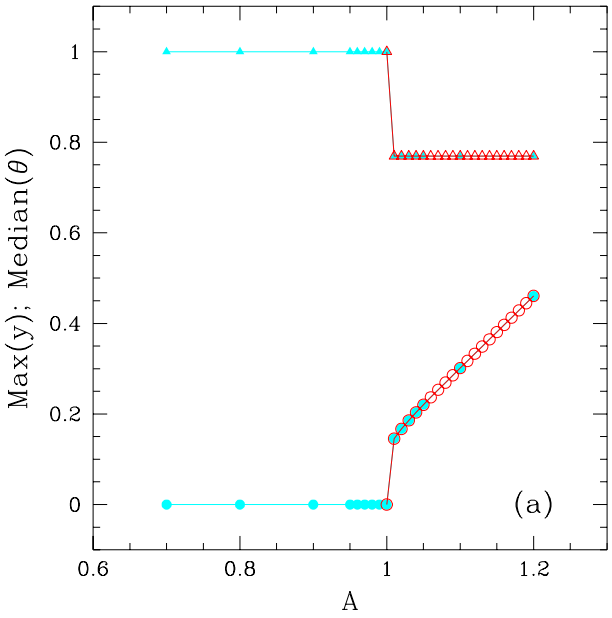

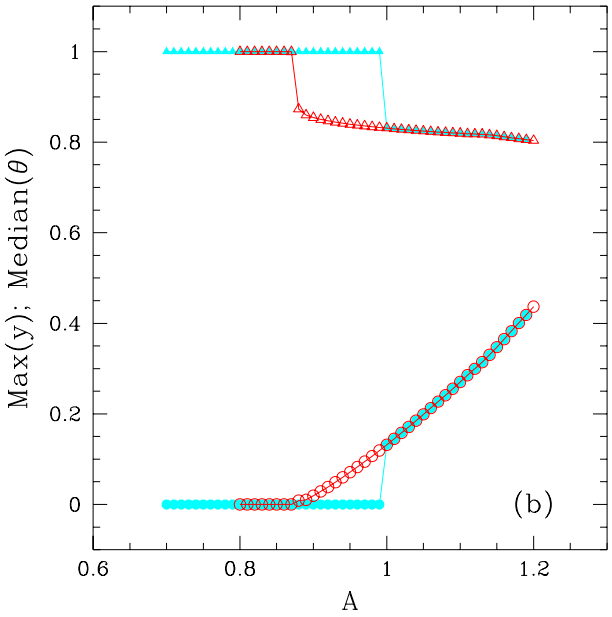

FIG. 24. Comparison of the transitions near failure for (a) the simple Coulomb model (instantaneous switching of friction coefficient) and (b) an improved model with relaxational switching. The data show the maximum velocity, y (circles) and the median value of the friction coefficient, θ (triangles). Closed symbols are for increasing shaking amplitude A; open symbols are for decreasing A. Model parameters are $W = 0$, $\tau = 10^{-6}$ in (a) and $W = 10^{-4}$, $\tau = 10^2$ in (b).

We compare results computed for the simple Coulomb case and the relaxation model in Fig. 24. Note that in the Coulomb case, there is a discontinuous but reversible transition in the variables y and θ when the amplitude A is increased past the failure point. By contrast, with the relaxation model, the transition is hysteretic. To demon-

strate this more clearly, we show in Fig. 25 a blowup of the region near the transition for the relaxational model.

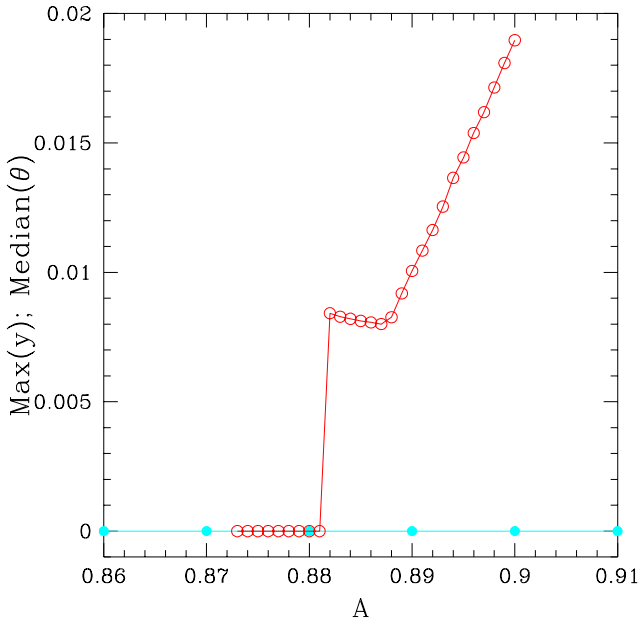

FIG. 25. A blowup of the transition region in figure 24 for the relaxational friction model. Closed symbols are for increasing shaking amplitude A; open symbols are for decreasing A.

VII. DISCUSSION AND CONCLUSIONS

The present experiments have probed the dynamics of the state change between a solid granular layer and a fluid granular layer using horizontal shaking. Under ordinary circumstances, this transition is backward, i.e. hysteretic. When the whole layer of material is shaken, the following scenario describes the onset of the instability and the mechanism for all aspects of the flow, including the cross-convective flow. The flow begins when the grains overcome frictional and dilatancy effects. The fluidized part of the layer exhibits strong back-and-forth sloshing. As a consequence of the sloshing, the material builds up on one side of the container and opens a trough on the opposite side; this process switches each half cycle. Grains fall into the trough during part of the motion, and this leads to a convective flow along the direction of shaking. For this component of the flow, grains on the surface flow away from the center, and are then reinjected from below. As a consequence of the sloshing, there is a shear flow of surface grains relative to the side walls ($x-y$ planes). Near these side walls, there is a strong dilatancy of the moving grains, due to the shearing. The grains in this highly dilated region near the side wall are mobile, and tend to percolate downward. (It seems likely that a similar phenomena occurs whenever there is shear at a sidewall.) However, grains falling along these walls are pushed inwards, and eventually they reach the surface again, towards the middle of the container. This leads to the heaping and the resultant flow back towards the side walls.

This work has uncovered several surprises. Perhaps the most striking is that if a slight overburden is added, the nature of the transition is substantially changed from backward/hysteretic to forward/nonhysteretic. In the absence of an overburden, the failure occurs locally, rather than over an extended surface, as suggested by classical Mohr-Coulomb models. This seems like a significant departure from conventional wisdom, and deserves deeper understanding. At present, we can offer the suggestion that surface effects, possibly associated with the thin layer of gas-like sliders plays an important role, although the details of the mechanism are not clear. It is possible that the slight overburden makes the layer more uniform, and hence more like the Coulomb picture. Also unexplained is the mechanism that sets the thickness of the fluid layer.

In related experiments, we have found that the hysteresis is also lifted by gentle fluidization. If roughly 40% of the weight of the material is supported by gas flow, the hysteresis at the fluid-solid transition is removed, and the transition point is lowered significantly.

Near the transition points in the hysteretic case, the times to generate the fluid or solid state diverge as power laws of the form $\tau = A|\epsilon|^{-\beta}$, where the exponent appears to be universally $\beta = 1.00$, within experimental error. This result suggests a common set of processes for the two directions of the transition. The exponent β for the fluid to solid transition is significantly elevated by the presence of a single more massive intruder particle.

Finally, we have tried to capture the phenomena observed in the experiments through simple friction models. These necessarily incorporate a lower friction coefficient, $\mu_k < \mu_s$ in the fluid versus the solid phases. However, this difference in friction coefficients is inadequate to capture the dynamics of the transition, especially the hysteresis. To describe this feature, we propose a simple model that allows for a time evolution of these coefficients from one state to the other. This model correctly predicts hysteresis at the transition.

[1] R. Behringer, H. Jaeger, and S. Nagel eds. Focus Issue on Granular Materials, *Chaos* **9**, 509–696 (1999) and articles following; H.J. Herrmann, J.-P. Hovi, and S. Luding, eds. *Physics of Dry Granular Media*, NATO ASI Series, Kluwer, 1997; R.P. Behringer and J.T. Jenkins, eds. *Powders and Grains 97*, Balkema, 1997; Y. Kishino, ed. *Powders and Grains 2001*, Balkema, 2001; H. M. Jaeger, S. .R. Nagel, and R. P. Behringer, Rev. Mod. Phys.

68, 1259 (1996); *Physics Today*, **49**, 32 (1996); See also R. P. Behringer, Nonlinear Science Today, **3**, No. 3, 1-15, (1993); A. Mehta, Ed. *Granular Matter: An Interdisciplinary Approach*, Springer, NY (1994); H. M. Jaeger and S. R. Nagel, Science **255**, 1523 (1992).

[2] R. Jackson, in *Theory of Dispersed Multiphase Flow, Ed. Re. E. Meyer* (Academic Press, NY, 1983, p. 291; R. M. Nedderman, *Statics and Kinematics of Granular Materials*, Cambridge, 1992.

[3] P.K. Haff, J. Fluid Mech. **134**, 401 (1983); J.T. Jenkins and M.W. Richman, Phys. of Fluids **28**, 3485 (1985); C.K.K. Lun and S.B. Savage, Acta Mechanica **63**, 15 (1986).

[4] S.B. Savage, J. Fluid Mech. **377**, 1 (1998).

[5] S.G.K. Tennakoon, L. Kondic, and R.P. Behringer, Europhysics Lett. **45** 470–475 (1999).

[6] M. Medved, D. Dawson, H.M. Jaeger, and S.R. Nagel, CHAOS **9** 691 (1999).

[7] C. Salueña, T. Pöschel, and S.E. Esipov, Phys. Rev. E **59**, 4422 (1999).

[8] P. Evesque, Contemporary Physics **33**, 245 (1992).

[9] O. Pouliquen, M. Nicholas, and P. D. Weidman, Phys. Rev. Lett. **79**, 3640 (1997).

[10] K. Liffman, G. Metcalfe, and P. Cleary, Phys. Rev. Lett. **79**, 4574 (1997).

[11] G. H. Ristow, G. Straßburger, and I. Rehberg, Phys. Rev. Lett. **79**, 833 (1997).

[12] PCB Piezotronics, 3425 Walden Ave. Depew, New York 14043, USA.

[13] H. K. Pak and R. P. Behringer, Phys. Rev. Lett. **71**, 1832 (1993).

[14] E. van Doorn and R. P. Behringer, Phys. Lett. A. **235**, 469 (1997).

[15] Reynolds, O., Phil. Mag., **20**, 469 (1885).

[16] G. S. Grest and K. Kremer, Comp. Phys. Comm. **55**, 269 (1989).

[17] P. A. Thompson and G. S. Grest, Phys. Rev. Lett. **67**, 1751 (1991).

[18] S. Luding, in *Physics of Dry Granular Media*, Ed. H. J. Herrmann, J.-P. Hovi, and S. Luding, (Kluwer Academic Publishers, Dordrecht) (1998).

[19] However, since the force on the wall particles is not calculated, this approach does not use significant additional computational resources.

[20] S. Luding, E. Clement, A. Blumen, J. Rajchenbach, and J. Duran, Phys. Rev. E **50**, 4113 (1994).

[21] Y. Zhang & C.S. Campbell, J. Fluid Mech. **237** 541–568 (1992).

[22] J. M. Carlson and A. A. Batista, Phys. Rev. E **53**, 4153 (1996).